

RESEARCH ARTICLE

Making powder aerosol deposition accessible for small amounts: A novel and modular approach to produce dense ceramic films

Jörg Exner  | Mario Linz | Jaroslaw Kita  | Ralf Moos 

Department of Functional Materials,
University of Bayreuth, Bayreuth,
Germany

Correspondence

Jörg Exner and Ralf Moos, Department of
Functional Materials, University of
Bayreuth, Bayreuth, Germany.
Email: Functional.Materials@Uni-
Bayreuth.de

Funding information

Funding from the Deutsche
Forschungsgemeinschaft (German
research foundation, DFG) is gratefully
acknowledged (DFG grant MO
1060/40-1).

Abstract

Powder aerosol deposition is a promising technique to deposit dense ceramic films directly at room temperature. While previous developments pointed towards larger and more complex deposition devices, this work follows a different approach and proposes a simplified and miniaturized coating device (denoted as Micro-PAD, μ PAD). The aim is twofold: creating a smaller and flexible device consisting of an aerosol generation unit and a deposition chamber with a combined low areal footprint of 30 cm by 20 cm (that, e.g., easily fits in a glove box) as well as lowering the hurdle for other researchers to use the powder aerosol deposition. Therefore, we introduce a device mainly based on commercially available components/connectors as well as manual operated valves/flow meters. A key point is the elimination of moving components by just using a spot deposition that was enabled by using a circular de-Laval-type nozzle.

The operational capability of μ PAD is proven for the deposition of alumina films and compared to conventional PAD in terms of mechanical, crystalline, and optical film properties. Thick films with a bell-shape-like profile are deposited by μ PAD, featuring a plateau in the center of the film with a diameter of 5 mm and a FWHM (full width at half maximum) diameter of about 10 mm. Alumina films produced by μ PAD do not only match the properties of corresponding PAD films, but oftentimes outperform them. Here, μ PAD films exhibit increased hardness and optical transmittance values, surpassing reference values of the conventional sprayed counterparts by at least 10%. Also, film integrity and adhesion to the substrate are slightly higher in case of μ PAD. Reasons for the improved film properties are found by X-ray diffraction, with a significantly higher fracturing of impacting particles during μ PAD combined with improved film consolidation as observed by SEM. Furthermore, μ PAD featured doubled to tripled the deposition rates and, markedly almost doubled the deposition efficiency.

KEYWORDS

ceramic cold processing, ceramic spray coating, miniaturized deposition device, optical transmittance, spot deposition

This is an open access article under the terms of the [Creative Commons Attribution-NonCommercial-NoDerivs](https://creativecommons.org/licenses/by-nc-nd/4.0/) License, which permits use and distribution in any medium, provided the original work is properly cited, the use is non-commercial and no modifications or adaptations are made.

© 2021 The Authors. *International Journal of Applied Ceramic Technology* published by Wiley Periodicals LLC on behalf of American Ceramics Society

1 | INTRODUCTION

Ceramic films are of high interest in a broad variety of technical applications, ranging from high-temperature-resistant, abrasive, and chemically stable protective films over electrically insulation films to applications as functional components in solid oxide fuel cells, lithium ion batteries, or sensors. It is a major drawback for many ceramic films that typically very high production temperatures either during or after film formation are required to form the dense and suitable ceramic (micro)morphology. Two exemptions exist that may overcome this requirement: cold sintering¹ and aerosol deposition method.² While the first technique is mainly utilized to manufacture bulk samples,³ the latter enables to produce dense ceramic films without any heat treatment directly at room temperature.⁴ Aerosol Deposition (abbreviated as AD or ADM),⁵ oftentimes also referred as powder aerosol deposition (PAD),⁶ vacuum kinetic spray (VKS),⁷ or vacuum cold spray (VCS),⁸ is a dry ceramic powder spray-coating method that uses micrometer-sized powders (0.5–5 μm).² For all methods, dry ceramic particles are accelerated to velocities in the range of 150–500 m s^{-1} in a carrier gas flow of 1–20 L min^{-1} . The particles subsequently collide with the surface that is to be coated in rough vacuum conditions ($p = 1$ mbar). Film formation and growth occur based on the *Room Temperature Impact Consolidation* (RTIC) mechanism by mainly using the kinetic energy of the impacting particles without dominating thermal heating effects.⁹ Upon high-momentum contact with the substrate, the particle undergoes a brittle fragmentation to nanometer-sized fragments in conjunction with plastic deformation.¹⁰ The newly formed fragments exhibit fresh, unsaturated and therefore reactive surfaces that bond to the substrate as well as to already deposited particles. An additional film densification emerges by subsequently impacting particles that consolidate the previously formed film. Already realized electrochemical applications are photocatalytic ceramics^{11–17} like TiO_2 , GaN-ZnO , and BiVO_4 , as well as energy storage and conversion devices like fuel cells,^{18–22} thermoelectric generators,^{23,24} and batteries.^{25–32} Furthermore, a variety of sensors was published using powder aerosol deposited functional films.^{33–38} A more detailed description of the aerosol deposition process, its deposition mechanism, and the resulting film properties can be found in overview articles of Akedo's group^{39,40} and of our group.²

Developments in the past decade pointed towards a better understanding of the deposition mechanism,^{10,41–44} possible applications,^{36,40,45–48} and a scale-up of the spray process.⁴⁹ The latter resulted in an enhanced process control and increased coating areas, for example, for PZT on 4-inch wafers,⁵⁰ SOFC anode/electrolyte bi-layers up to

1000 cm^2 ,⁵¹ Y_2O_3 transparent films on 500 mm square glass panels,⁵² and even larger films using nozzles width of 400 mm up to 1000 mm.^{49,53} However, this process improvement comes at the cost of a significantly raised complexity of the coating devices. Consequently, expensive moving stages, high-throughput aerosol generation devices, and very large deposition chambers are required. The high necessary investment costs and the difficult prospect to build the required knowhow may hinder researchers and developers in the field of chemistry, physics, and material science to start using this otherwise very promising coating technique. Furthermore, with existing PAD machinery, it is hardly possible to deposit newly synthesized materials that are often available in very small quantities below one gram.

To complement this, we have developed a simplified method that enables the room temperature deposition of powders, even if these are only available in small amounts. In other words, the aim of this modular and miniaturized approach, which we will denote as μPAD in the following, is to allow for a film formation on a smaller scale yet still adequate for material research and application testing. This will be shown for alumina, the best-investigated material for PAD. Alumina films produced by the proposed μPAD setup are characterized in terms of their mechanical, crystalline, and optical properties and are compared with conventionally sprayed PAD reference samples.

2 | EXPERIMENTAL DETAILS

For a proof of concept, alumina powders were used to determine the performance of conventional PAD and miniaturized Micro-PAD (μPAD) in terms of film deposition and film properties.

2.1 | Differences of a conventional PAD and the modular μPAD setup

A powder aerosol deposition apparatus typically consists of three main components: 1. a deposition chamber, 2. an aerosol generation unit including the aerosol chamber and the carrier gas supply, and 3. a high-throughput vacuum pump (as displayed in Figure S1 in the Supporting Information). The dry coating material is placed within the aerosol chamber. A defined carrier gas, which is electronically controlled by mass flow controllers, is injected into the aerosol chamber. Thereby, the powder becomes airborne and forms a fluidized bed. A mechanical vibration supports the formation and stability of the aerosol generation. A constant pressure difference between the aerosol chamber and the deposition chamber

is maintained by continuous evacuation of the deposition chamber through the vacuum pump. Consequently, particles are transported through the connecting pipe and get accelerated by a nozzle. In most PAD setups, stationary slit nozzles with widths between 5 and 1000 μm are used. To form a ceramic film of a certain size, the substrate is repeatedly scanned above the nozzle by a predefined motion sequence of the motorized x - y stage. A scheme of the section within the conventional PAD chamber containing the slit nozzle, the substrate, and the substrate mounting is shown in Figure 1A.

In general, the same main components are present in μPAD equipment, too. However, in this work, we focus on the aerosol generation unit and the deposition chamber. A vacuum pump as third component is also required to operate the device yet will not be part of the thorough discussion since it is a commercially available standard part. The main difference between μPAD and PAD is undoubtedly the absence of moving parts like the before-mentioned x - y stages. Therefore, the deposition area is reduced to nearly the size of the nozzle orifice (see Figure 1B). Hence, converging slit nozzles become unfavorable since an irregular-shaped, line-like film forms. To overcome this issue and to allow for the deposition of uniform film areas, de-Laval-type nozzles with a circular orifice are used instead. Each deposited film (spot) thereby also exhibits a circular appearance, preferably featuring a plateau with constant thickness in the center of the spot. More detailed design principles are also given in the Supporting Information

(Section: *general design principles of the μPAD setup*). After explaining the idea of the μPAD setup, the exact layout and used components are described in the following.

The realized, compact μPAD device (excluding the vacuum pump) as well as a scheme of it are shown in the images of Figures 2 and 3, respectively. A detailed 3D model is also available in the Supporting Information (Figure S2). Commercially available small flange components (ISO-KF, Pfeiffer Vacuum) were chosen to construct the modular deposition chamber. KF40 with an inner diameter of 40.5 mm was identified as the best trade-off between miniaturization and cleanability on one hand as well as operability and low gas flow resistances on the other hand.

The main deposition chamber on the right-hand side in Figure 2A consists of a low-profile, angular-shaped KF40-Tee and houses the de-Laval-type nozzle. A blank flange with an aerosol feedthrough (bulkhead union; Swagelok, outer diameter of 6 mm, inner diameter of 4 mm) is located at the top side of the chamber while the exhaust to the vacuum pump is attached to the side port. The latter connection can be closed using a KF40 butterfly valve and may be implemented with a corrugated KF40 hose for more flexibility. The third port optionally extends the deposition chamber downwards with KF40 pipes or can be sealed using a blank flange. Here, two different modes of operation exist: Either the substrate is small enough to fit inside the inner diameter of the pipe and therefore a completely closed chamber is preferred, or a semi-open chamber may be used for large substrates exceeding sizes of 45 mm. The latter option requires a flat and mechanical stable substrate that represents the last wall of the deposition chamber therefore fully sealing it. This setup is displayed in Figure 2 and in Figure S2 with a square substrate of 100 mm edge length.

The aerosol formation is achieved in a custom-made, lab-scale aerosol chamber as displayed in Figure 2B. It consists of three connecting ports. Here, the glass aerosol chamber also houses a horizontal porous glass frit near the lower end, which allows to permit a gas flow while restricting the powder to the upper part of the chamber. A gas flow, denoted as aerosol inlet gas flow, enters through the lower port of the chamber, passes through the porous frit, and aerosolizes the coating material. Airborne aerosol continuously flows to the top of the aerosol chamber, is ejected through the upper connector (see yellow arrow), and is mixed with a dilution gas flow (upper green arrow). A flexible tube transports the aerosol to the miniaturized deposition chamber, where it gets accelerated within the de-Laval-type nozzle and subsequently gets deposited. The third port at the aerosol chamber connects to a pressure gauge to monitor the process pressure level. When unplugging this connector, refilling of the aerosol chamber is possible using a funnel.

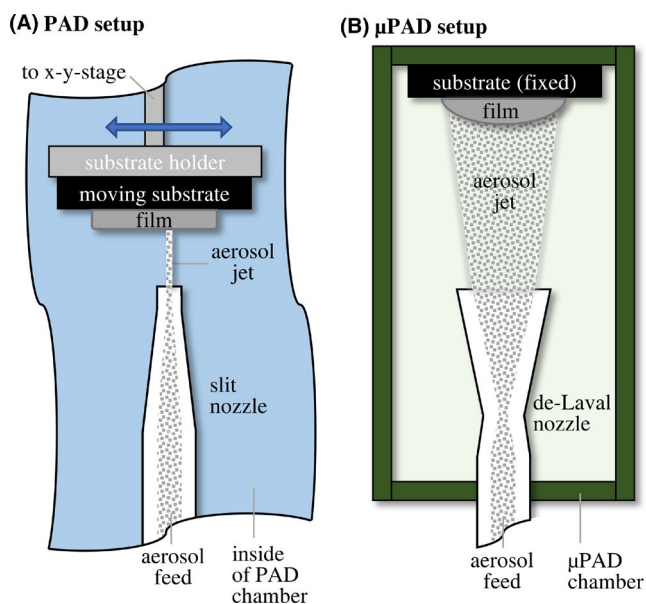


FIGURE 1 Schematic representation of spray setups used in (A) conventional PAD and (B) μPAD . Shown is the section depicting nozzle, formed aerosol jet, substrate and substrate mounting [Color figure can be viewed at wileyonlinelibrary.com]

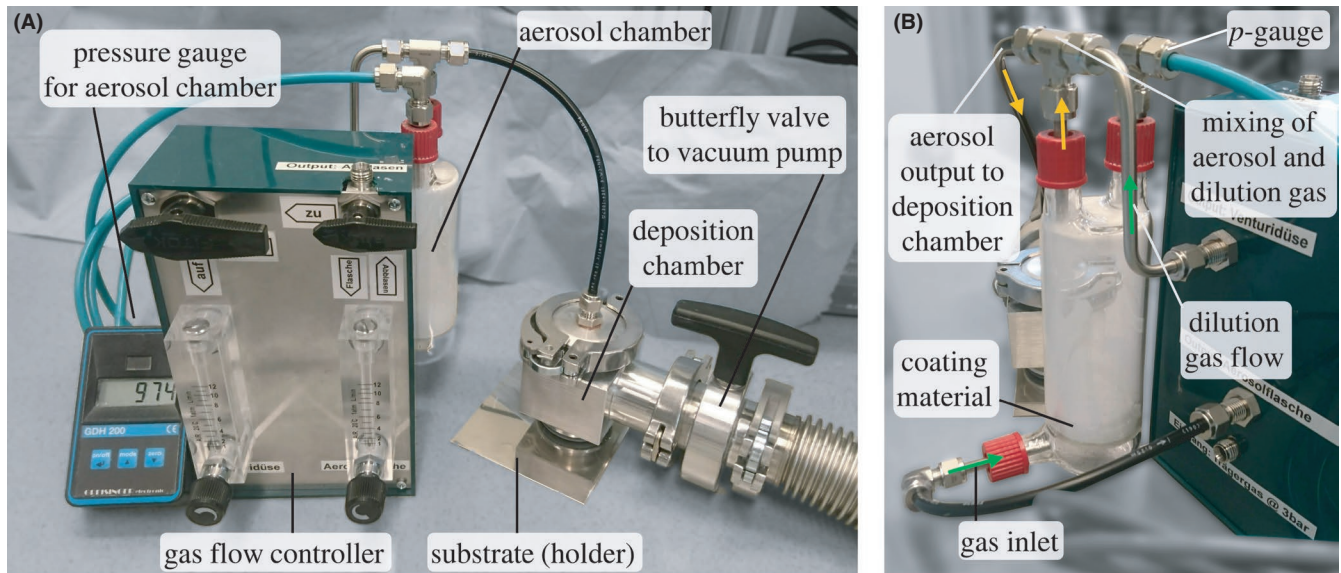


FIGURE 2 Image of the proposed modular μ PAD apparatus used for spot deposition: (A) front view of the complete setup and (B) back view depicting the aerosol chamber and the aerosol/gas flows (green arrows indicate gas flows while yellow arrows indicate aerosol transport) [Color figure can be viewed at wileyonlinelibrary.com]

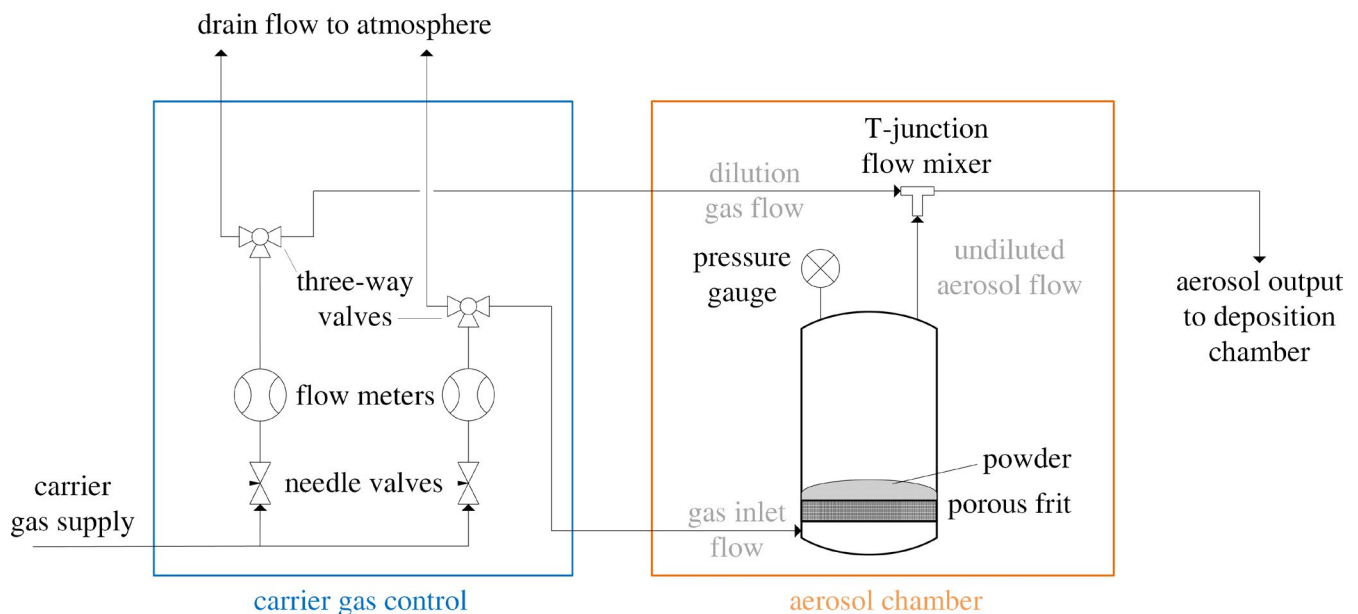


FIGURE 3 Schematic representation of the aerosol generation unit consisting of the carrier gas control and aerosol chamber [Color figure can be viewed at wileyonlinelibrary.com]

The complete aerosol chamber is top-mounted, hanging at the dilution gas flow pipe of the gas flow controller box. Therefore, the lower end of the aerosol chamber remains movable to a certain degree and allows for a mechanical shaking of the device (e.g., using an attached unbalance vibrator). This supports the formation of the fluidized powder bed and enhances the stability of the aerosol output. By using two gas flows—the aerosol inlet flow and the dilution gas flow—the aerosol concentration (mass of powder per time) may be altered independently

of the additional important spray process parameters (especially the total gas flow responsible for the aerosol acceleration within the nozzle). Both flows are independently adjustable using two sets of flow meters with attached needle valves (Figure 3) integrated in a flow controller box. Since gas flows in PAD are typically given in standard liter per minute measured against ambient atmosphere, three-way valves enable to switch among three states to control the process: 1. closed—no gas flow (*no deposition*), 2. drain flow to atmosphere to adjust the desired gas flow

rates (*no deposition*), and 3. gas and aerosol flow to deposition chamber (*active deposition*).

The last preliminary study investigates the pressure in the deposition chamber since it is one of the most crucial PAD parameters (see Supporting Information, Figure S3). In contrast to conventional PAD deposition chambers with large piping profiles, μ PAD shall utilize smaller and flexible hoses to connect the chamber to the high-throughput vacuum pump. Typical flow rates for PAD are in the range of 5–10 L min⁻¹, leading to a chamber pressure of 0.4 to 0.8 mbar (based on the pump characteristics of a 1000 m³ h⁻¹ pump system). For the μ PAD setup using the proposed flexible KF40 hose, here with a length of 0.75 m, the working pressure range rises by a factor of 2 (0.8–1.7 mbar) due to increased flow resistances. However, this pressure still coincides well with the typically used value of about 1 mbar for PAD.⁵⁴ If a corrugated hose with only a diameter of 25 mm (KF25) and a length of 1 m were used instead, pressure levels again would grow to 2.1 to 4.1 mbar. This is significantly higher than 1 mbar, yet still falls in the often stated deposition pressure region between 0.2 and 20 mbar that is suitable for PAD.^{2,39} To stay as close as possible to optimal PAD process parameters, the larger KF40 hoses were used for the coating runs.

2.2 | Film preparation

Alumina films were prepared using the described μ PAD setup and compared to reference samples produced by conventional PAD as described in previous publications.^{38,55}

All process parameters are summarized in Table 1. For good comparability, matching deposition parameters were chosen as far as possible. The same two-stage vacuum pump, aerosol generation chamber, alumina powder (Sasol Chemicals LLC), and substrates were used. With standard spray parameters, PAD films with an area of 10 × 10 mm² (see Table 1), with 8–60 scans each resulting in coating durations t_c of 15 to 120 s were manufactured.

Differences occurred mainly due to the different operation modes of PAD and μ PAD. While for PAD, a standard slit nozzle that requires an x - y movement of the substrate to obtain a rectangular-shaped film (including masking of the turning points of the scan movement) was applied, μ PAD uses a single-spot deposition with a stationary substrate. Hence, an adapted nozzle geometry became necessary. A round de-Laval-type nozzle (orifice: $\varnothing = 10$ mm, throat: $\varnothing = 3.5$ mm, material: ABS) was used. The μ PAD spray parameters were set to obtain an identical aerosol chamber pressure of 210 mbar. Due to the different nozzle geometry, the total oxygen carrier gas flow had to be adapted from 6 to 8 L min⁻¹, divided into 6 L min⁻¹ to the aerosol chamber (identical to conventional PAD) and additional 2 L min⁻¹ as dilution gas flow. Consequently, the deposition chamber pressure slightly increased from <1 to 1.4 mbar. The used nozzle exhibited an increased substrate-to-nozzle working distance of 55 mm and created bell-shape-like film profiles with diameters of about 10 mm (FWHM, full width at half maximum).

All produced films including important spray parameters, resulting film thicknesses h , and deposition efficiencies are summarized in detail in Table S1 (Supporting

TABLE 1 Spray parameters used for conventional PAD and μ PAD

	Conventional PAD	μ PAD
Aerosol generation unit	Custom-built fluidized bed aerosol generator	
Nozzle	converging slit nozzle orifice: 10 × 0.5 mm	de-Laval-type round nozzle orifice: $\varnothing = 10$ mm throat: $\varnothing = 3.5$ mm
Distance nozzle – substrate	2 mm	55 mm
Carrier gas flow	6 L min ⁻¹ O ₂	6 L min ⁻¹ O ₂ (aerosol unit) + 2 L min ⁻¹ O ₂ (dilution)
Pressure aerosol chamber	210 mbar	210 mbar
Pressure deposition chamber	<1 mbar	1.4 mbar
Substrate scan velocity	5 mm s ⁻¹	None–spot deposition
duration of coating t_c	15 to 120 s (8 to 60 scans)	15 to 120 s
Film area	Rectangular, 10 mm × 10 mm	Circular, bell-shaped profile $\varnothing \approx 10$ mm (FWHM)
Substrate masking	Turning points of scanning	None
Coating material	Al ₂ O ₃ powder (Sasol Chem., $d_{50} = 0.9$ μ m, sieved and dried)	
Substrate material	Stainless steel, glass, and silicon (the latter for obtaining XRD patterns)	

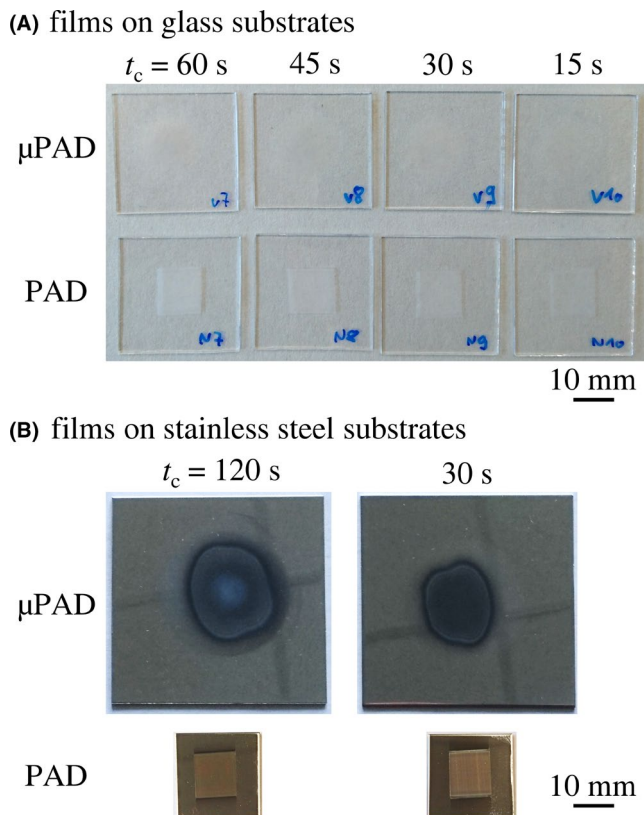


FIGURE 4 Images of alumina films produced by PAD or μ PAD after different coating durations t_c on (A) glass substrates and (B) stainless steel substrates [Color figure can be viewed at wileyonlinelibrary.com]

Information). Figure 4 shows the images of sprayed films on glass and on stainless steel substrates after different coating times t_c .

A difference in the film areas is well noticeable with a rectangular shape for the PAD films in contrast to the circular appearance of the μ PAD films. However, the edges of μ PAD films are optically less distinctive compared to PAD films, probably due to a more gradual incline of the μ PAD film profile instead of the steep film flanks observed in PAD films. For both coating methods, alumina films on glass substrates exhibit a pronounced transparency for shorter coating durations. This observation is later discussed in detail based on the optical transmittance and film thickness measurements.

2.3 | Film characterization

X-ray powder diffraction (XRD) patterns (D8 Advance, Bruker, Ge-K α 1 monochromator) were taken from the applied powders and the sprayed films on silicon between 20° and 70° (2θ) in steps of 0.02° for a hold time of 0.5 s each. *X'Pert HighScore Plus* software was used for structure verification. The patterns were compared with the hexagonal alpha alumina pattern (ICDD-PDF 04-004-2852).

To determine the crystallite size and the internal strain, Rietveld refinement was conducted using the *TOPAS-Academic* software. A differentiation of crystallite size and strain is possible, since both effects depend differently on the Bragg angle θ of the reflection.⁵⁶ The crystallite size depends on $1/\cos(\theta)$, whereas the microstrain depends on $\tan(\theta)$.

To investigate the film morphology, samples on stainless steel substrates were prepared for cross-sectional imaging (embedded in resin followed by grinding and mechanical/chemical polishing) on a scanning electron microscope (Leo 1530 VP, Zeiss).

The thickness h of all deposited films was measured by a stylus profilometer (Jenoptik Waveline W20). 3D surface profiles of selected μ PAD and PAD films were taken using a 405-nm laser scanning confocal microscope (LSM 900 Mat, Zeiss) to determine three-dimensional film thickness profiles and profile roughness parameters.

The hardness of the samples on stainless steel substrates was determined by a microindentation hardness tester (Fischerscope HM2000, Fischer Technology Inc.) in accordance with DIN EN ISO 14577 1-3. Here, 25 indentations with a force of 100 mN were repeated for each sample and the averages were calculated.

The optical (in-line) transmittance of films on glass substrates was determined between 250 and 1050 nm by a UV-Vis-NIR spectrophotometer (Cary 60, Agilent). As reference, an uncoated glass substrate was measured. The following parameter set was used for all transmittance measurements: scan rate = 600 nm/min, data interval = 1 nm, and average time = 0.1s.

To investigate the mechanical stability and adhesion of the deposited films, Daimler-Benz Rockwell-C adhesion tests were conducted on films on stainless steel. This technique enables a semi-quantitative statement about the adhesion and general mechanical integrity of coated components (in accordance with the German VDI 3198 standard).^{57,58} The investigation follows the indentation procedure of a Rockwell-C hardness measurement, followed by an optical assessment around the imprint by light microscopy. A conical indenter yields a massive plastic deformation within the coating and substrate, combined with extreme shear stresses at the interface of both. General adhesion is described in six quality levels ranging from HF1 (tight bonding to the substrate) to HF6 (low adhesion with catastrophic failure and excessive delamination). Classification is based on the amount of visible crack formation and film delamination around the circumference of the indentation spot, as summarized in the schematic test chart in Figure S6 (Supporting Information).⁵⁹ Only HF1 to HF4 are considered as acceptable failure modes, whereas HF5 and HF6 indicate a poor adhesion with a widespread and (nearly)

entire peeling of the coating. For high quality coating with HF1 and HF2, solely minor cracks without any delamination are tolerated. HF1 and HF2 are distinguished by the number of occurring cracks: when only a few without the formation of a crack network exist, it is considered as the highest quality level HF1. The Daimler-Benz Rockwell-C adhesion test is limited to film thicknesses up to 5 μm and to ductile substrates that withstand the high indentation forces. Four to six spots were measured for each investigated sample using a Wolpert hardness measurement system (120° conical diamond indenter; 150 kg load with 15-s holding time).

Two important key performance indicators of PAD are the deposition rate r_c and the deposition efficiency η_c . The deposition rate r_c describes the deposited volume V_c per coating time t_c

$$r_c = \frac{V_c}{t_c}. \quad (1)$$

r_c is typically given in $\text{mm}^3 \text{min}^{-1}$ or $\mu\text{m} \text{mm}^2 \text{min}^{-1}$. The deposition efficiency η_c given in % indicates the ratio between deposited film mass m_c and the mass of the sprayed powder m_{powder}

$$\eta_c = \frac{m_c}{m_{\text{powder}}}. \quad (2)$$

3 | RESULTS AND DISCUSSION

Alumina films produced by conventional PAD and by μPAD were comprehensively characterized in terms of their mechanical, crystalline, optical, and surface profile film properties. The overall aim is to survey whether with the proposed miniaturized and simplified μPAD setup films with a similar quality of conventionally sprayed PAD films can be obtained.

3.1 | Surface and profiles of films

Shape and homogeneity of deposited films are important factors for their later application. Films deposited on both

stainless steel and glass substrates were analyzed with the laser scanning microscope. Films with the longest coating duration t_c of 60 and 120 s, respectively, and high powder fillings of 13 g and higher were characterized. Table 2 summarizes the mean thicknesses h and volumes V_c , as well as roughnesses R_a (centerline-average) and R_z (maximum height of the profile) of these films.

Looking at the films on stainless steel, it is obvious that the deposition by μPAD achieves a significantly higher mean film thickness of 26 μm over 11 μm for conventional PAD. On glass substrates, the thickness increases by a factor of 3 to 4 (11 μm for μPAD in contrast to about 3 μm for PAD). Since the shape of the films is different, as discussed above, the deposition rate r_c calculations are based on the complete film volume V_c instead of just the film thickness h . However, the previous observations are also roughly valid for the behavior of r_c , with $r_c = 1.1 \text{ mm}^3 \text{min}^{-1}$ and $r_c = 0.92 \text{ mm}^3 \text{min}^{-1}$ for μPAD on steel and glass, respectively, in contrast to $r_c = 0.55 \text{ mm}^3 \text{min}^{-1}$ and $r_c = 0.33 \text{ mm}^3 \text{min}^{-1}$ for conventional PAD. This indicates that the volumetric deposition rate r_c is almost tripled in case of μPAD under otherwise closely matching spray parameters. Much of that differences may be explained by a change in the weight-based deposition efficiency η_c . Here, processing by μPAD yields η_c about 0.2%, while with PAD only 0.1% is reached. The latter behavior coincides well with deposition experiments by Naoe et al. They used a similar rectangular nozzle (orifice 10 mm \times 0.4 mm) with a deposition efficiency for alumina particles of up to 0.10%.^{60,61} Undeniably, η_c is still quite small for μPAD and PAD alike, meaning that 99.8% of the used alumina powder does not participate in film formation and typically settles within the deposition chamber. A reuse of the loosely adhered, undeposited powder was possible in preliminary, yet to be published experiments. This indicates that the low η_c of single deposition experiments may be considerably improved through multiple usage.

When comparing the R_a and R_z roughness values of μPAD films with their PAD counterpart (see Table 2), μPAD films tend to be rougher. However, the film thicknesses should be taken into account when interpreting roughness values of PAD films. As already described by Lee et al., the mean roughness R_a of alumina PAD films increases with

TABLE 2 Film thickness, volume, and roughness of PAD and μPAD films on steel and glass substrates, respectively

Process	Substrate	Coating time	Film thickness	Film volume	Film roughness	
		t_c	H	V_c	R_a	R_z
PAD	Steel	120 s	11 μm	1.11 mm^3	0.08 μm	0.54 μm
	Glass	60 s	3 μm	0.33 mm^3	0.05 μm	0.40 μm
μPAD	Steel	120 s	26 μm	2.27 mm^3	0.14 μm	0.84 μm
	Glass	60 s	11 μm	0.92 mm^3	0.08 μm	0.55 μm

film thickness.⁶² Their reported data showed an increase in the mean roughness from 0.07 to 0.12 μm when films grew from 0.5 to 3 μm . This behavior, however, seems to be dependent on the used alumina powder and its particle size, since the same group published contradictory results where higher scanning numbers (and therefore higher film thicknesses) yielded decreasing film roughnesses.⁶³ By coincidence, the μPAD film on glass ($t_c = 60$ s) and the PAD film on stainless steel ($t_c = 120$ s) exhibit matching film thicknesses of 11 μm , therefore enabling to directly compare the roughness of μPAD versus PAD. Both films, independent of the type of manufacturing, feature identical roughnesses of $R_a \sim 0.08$ μm and $R_z \sim 0.55$ μm .

After explaining the general deposition characteristics in terms of film thickness and deposition rate, the resulting film profile is investigated in detail. Figure 5 shows the three-dimensional film thickness of the PAD reference

sample on the stainless steel substrate together with two line profiles perpendicular and parallel to the substrate traverse direction. For the conventionally sprayed reference samples, the following orientation applies: The long side of the slit nozzle orifice with a length of 10 mm is oriented perpendicular to the traverse direction; hence, Figure 5B represents the film thickness distribution along the nozzle length. The profile parallel to the traverse direction in Figure 5C illustrates the timely homogeneity of the film deposition. Please note that only the reversal points of the movement (meaning the front and back side of Figure 5A) were masked during deposition, which was not the case for the sides of the film.

The sprayed reference PAD film features a nearly flat plane in the center of the film with a thickness of 11.5 μm , whereas the left and right boundaries are slightly elevated to about 17 μm . This film thickness distribution is caused by the used slit nozzle (details are given in the Supporting Information). Along the traverse direction, the film thickness is nearly constant with a low standard deviation of 0.5 μm . The shape of the PAD film prepared on the glass substrate (see Figure S4 in the Supporting Information) coincides, in general, with the film on stainless steel; however, due to a shorter coating time and less amount of used powder for the deposition, the thickness is lowered to about 3.2 μm . Summarizing both samples produced by PAD, the deposition is generally independent on the substrate material and results in similar film appearances. The standard slit nozzle with an orifice of 10 mm \times 0.5 mm in combination with the alumina powder and the used spray parameter yields rectangular ceramic films with a nearly flat plateau at the center of the film and elevated film edges.

The shapes of the alumina films produced by the μPAD method deviate widely from the previous observed PAD films, as displayed in Figure 6 for the μPAD film on stainless steel. The thickness, in general, resembles a bell-shaped profile. Please note that due to the significantly miniaturized deposition chamber, the location of the vacuum chamber port becomes increasingly important. Looking at Figure 6A, the vacuum port was located at the back side of the sample (corresponding to the upper side of the top view inset in Figure 6B).

The thickness profile perpendicular to the vacuum port in Figure 6B shows an almost symmetrical course. In this measuring direction, the bell shape is flattened in the center of the film, resulting in a plateau with a height of 26 μm at a diameter of about 5 mm (the FWHM diameter is about 10 mm). Looking at the profile measured towards the vacuum port (Figure 6C), a non-symmetry occurs. While the side that faces the vacuum pump is elevated to 28 μm , the opposite side is reduced to 24 μm . This behavior may be explained by two major differences between the μPAD and

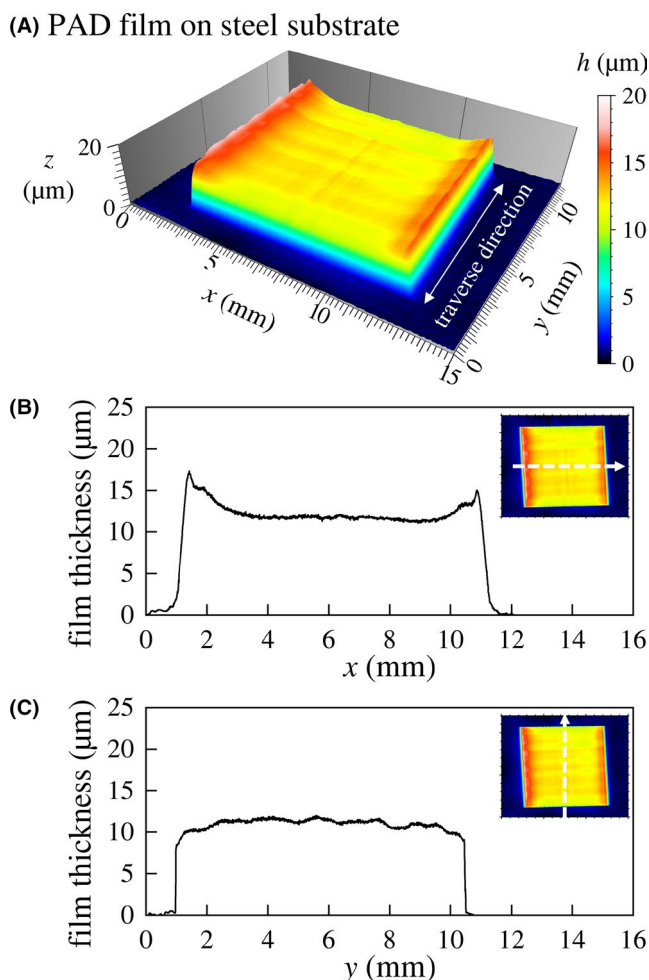


FIGURE 5 Surface profile of a conventionally sprayed PAD film on a steel substrate: (A) 3D representation and thereof extracted 2D line profiles (B) along the nozzle length x as well as (C) substrate traverse direction y . The dashed arrow within the insets depicts the extracted line [Color figure can be viewed at wileyonlinelibrary.com]

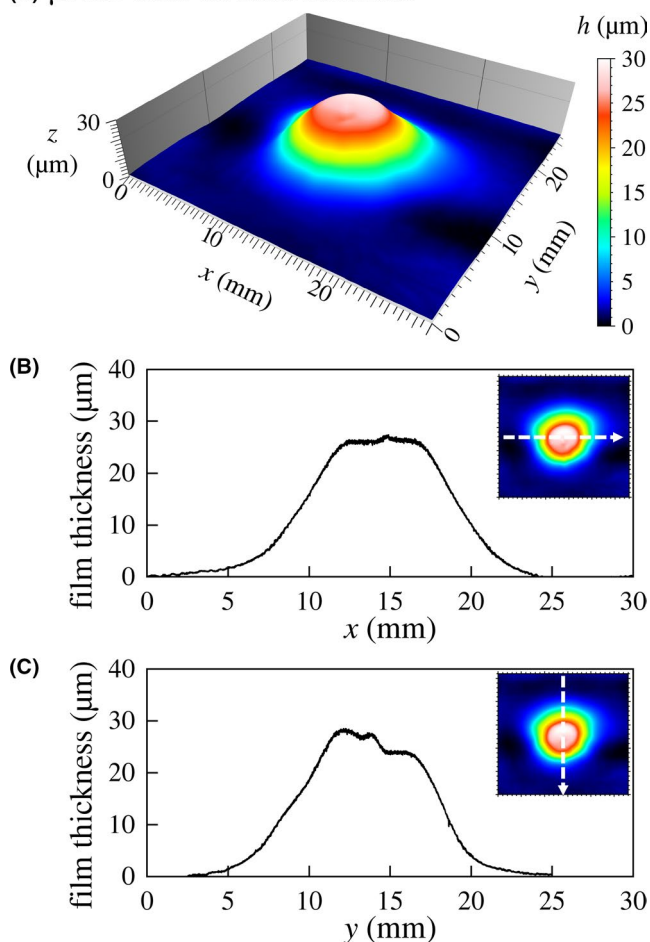
(A) μ PAD film on steel substrate

FIGURE 6 Surface profile of a spot sprayed μ PAD film on a steel substrate: (A) 3D representation and thereof extracted 2D line profiles (B) in perpendicular direction x to the vacuum port of the μ PAD chamber as well as (C) in parallel direction y . The dashed arrow within the insets depicts the extracted line [Color figure can be viewed at wileyonlinelibrary.com]

PAD chamber. Firstly, the miniaturized deposition chamber (KF40 pipe with inner diameter of 40.5 mm compared to inner chamber dimensions of 500 mm) may increase inhomogeneities of gas flow and pressure distribution, additionally influenced by the location of the vacuum port near the nozzle orifice (see Figure S2, Supporting Information). Secondly, the large nozzle-to-substrate distance of 55 mm, necessary for the de-Laval-nozzle, increases the time-of-flight of particles after ejecting from the nozzle orifice and hence results in a longer interaction time of particles and surrounding chamber gas before impacting the substrate. Consequently, the thickness distribution with about $26 \pm 2 \mu\text{m}$ is currently less uniform than for conventional PAD films. However, a derivation of about 8% may be tolerable in most applications and can be further decreased by an optimized μ PAD chamber design. When using glass instead of stainless steel as substrate,

the μ PAD film thickness again resembles a nearly circular, bell-shaped profile (Figure S5, Supporting Information). However, the total film thickness of $11 \mu\text{m}$ is lower due to the halved coating time of $t_c = 60 \text{ s}$.

To conclude, the μ PAD device allows for manufacturing spot-like ceramic films with a very simple and inexpensive setup. It additionally features higher deposition rates and efficiencies yet is limited in terms of coating areas at present. The homogeneity of the film thickness within the center (about 5 mm in diameter) is in the range of 4%–8% and is suitable for material research; however, film edges are significantly less steep due to the bell shape of the profile. Applying masks during deposition may allow for more precise edges, if necessary.

3.2 | Film morphology

Two sets of cross-sectional SEM images of alumina films on stainless steel produced by PAD and μ PAD, respectively, are shown in Figure 7. Both samples were produced using an identical coating time t_c of 120 s (see Table 2). The smallest magnification images in Figure 7A,D show uniform and defect-free thick films for both processing methods.

The thickness of the PAD film ($h = 11 \mu\text{m}$) perfectly coincides with the value previously determined using the laser scanning confocal microscope. For the μ PAD film, the thickness of $h = 18 \mu\text{m}$ is significantly higher compared to the corresponding PAD film; however, it appears lower than assumed in Section 3.1. The latter is probably related to the sample preparation with the cut slightly offset from the center of the film. Therefore, the cross-section does not display the center plateau of the film, yet a section of the falling edge of the bell-shaped film profile. Higher magnifications in Figure 7B,E reveal the high density and homogeneity of both films as well as their tight interface to the substrate. The interface between the substrate and the coating is not flat but has an irregular roughness due to the formation of the anchoring layer. However, the morphology of the PAD as well as the μ PAD film appear identical on this scale. Differences only emerge at the highest magnification, where the films' microstructure slightly differs. Please note that this nanogained structure is especially visible due to the chemical polishing of the cross-sectional samples leading to partially etched grains. The conventionally sprayed alumina film in Figure 7C consists of mainly two fractions: larger grains (crystallites) of 50 nm to 200 nm. They seem to be embedded in a matrix of even smaller grains of 20 to 30 nm. Additionally, nanopores of 10 to 20 nm are observed. In contrast, for the film produced by μ PAD in Figure 7F, almost no nanopores occur and the sizes and amounts of both grain

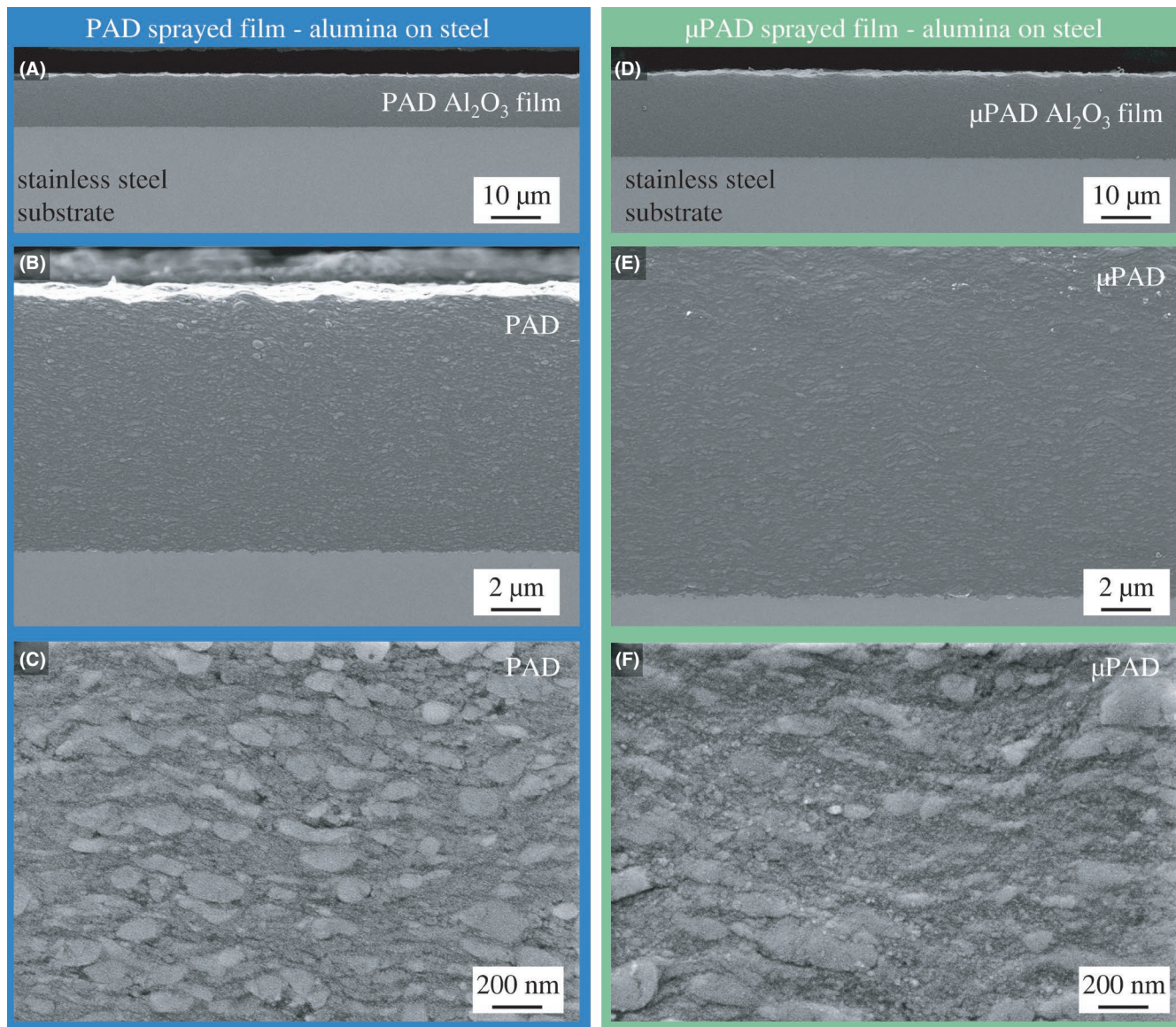


FIGURE 7 SEM cross-sectional images taken of (A–C) conventional sprayed PAD alumina films and (D–F) μ PAD processed alumina films [Color figure can be viewed at wileyonlinelibrary.com]

size fractions appear to be altered. Less volume is occupied by the larger grains and consequently the amount of the smaller grain fraction increases. Yet, sizes of a few single grains up to 300 nm significantly exceed those of the PAD counterparts. This indicates that a slight change in the deposition behavior of alumina particles occurs when using μ PAD in combination with its de-Laval-type nozzle. Higher particle velocities also increase the strain during particle impact, therefore affecting the formation of cracks and dislocations under fracturing.⁴⁴

The SEM images clearly demonstrate that the RTIC mechanism underlying PAD also takes place under the modified process conditions of μ PAD. The typical features of PAD including the dense and nanograined film morphology as well as the formation of the anchoring layer on ductile substrates are present within the μ PAD film.

Furthermore, the high-magnification SEM images even indicate an improved consolidation with less pores.

3.3 | Mechanical properties and film integrity

Ceramic PAD films usually are characterized by superior mechanical properties like hardness and film integrity (adhesion and stability). These properties are, therefore, an indication for a successful film formation, and hence, for the quality of sprayed films. Hardness values of two films on steel each produced by PAD and μ PAD, respectively, were measured using microindentation (Figure 8). Please note that higher amounts of powders and consequently higher aerosol concentrations were used for

the films with $t_c = 120$ s to achieve significantly higher thicknesses.

The 2.5 and 11- μm -thick PAD reference films exhibit a Vickers microhardness of 8.3 and 10.1 GPa, respectively. Both films produced by μPAD feature a higher hardness of 11.1 and 12.9 GPa at film thicknesses of 8 and 26 μm , respectively. Since there seems to be a tendency that higher film thicknesses lead to increased total measured hardness values, films with (approximately) similar thicknesses are compared. Here, even the 8- μm -thick μPAD film ($t_c = 60$ s) exceeds the hardness of the 3 μm thicker PAD film (11 μm , $t_c = 120$ s) by 10%. This shows that μPAD not only matches hardness values of conventionally sprayed PAD films but instead also outperforms them. All sprayed alumina films exhibit hardness values significantly higher than that of the used stainless steel substrate (2.2 GPa), indicating that measured values indeed originate from the contribution of the films. Sintered alumina substrates taken as reference range up to hardness values of 15 GPa and hence are slightly higher than the films. However, especially the 26- μm -thick μPAD films come considerably close to this bulk value.

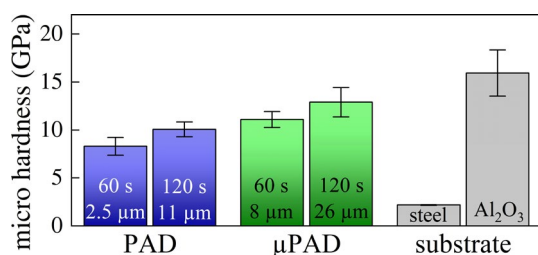


FIGURE 8 Vickers microhardness of alumina films produced by PAD and μPAD after coating durations t_c of 60 and 120 s. Measured bulk values of the used stainless steel substrate as well as bulk alumina are given for comparison [Color figure can be viewed at wileyonlinelibrary.com]

Film adhesion and integrity are analyzed using the Daimler-Benz Rockwell-C test in accordance with VDI 3198. Figure 9 shows optical microscope images of indentation spots on different samples. The uncoated steel substrate is shown as a reference (Figure 9A). Here, the ductile steel substrate clearly mirrors the imprint of the conical diamond indenter with a circular boundary to the non-deformed outer region. Selected indentation spots for the 2.5- μm -thick PAD alumina film and the 4.0- μm -thick μPAD alumina film are displayed in Figure 9B,C, respectively. The complete series of measurements with four to six spots per sample is available in Figure S7 (Supporting Information).

After the indentation procedure, both sample types still show a uniform coating outside the circumference of the imprint. Neither cracks nor delamination occur, also proving the superior quality and adhesion of PAD and μPAD films. In all cases, even the requirements for the highest adhesion level HF1 are easily surpassed, since HF1 still tolerates a few, isolated cracks ranging from the circumference into the undeformed film. Daimler-Benz Rockwell-C testing only makes use of the film appearance outside the imprint. Since both PAD and μPAD show undistorted, homogeneous surfaces after testing, the semi-quantitative method verifies that both film processing methods yield excellent mechanical properties. Therefore, high adhesion strengths are proven for the simplified μPAD , featuring this typical property of successfully deposited PAD films, too. Differences of the optical appearance between PAD and μPAD films yet are in the center of the imprint, within the circular boundary where highest mechanical stresses occur. Please note that studying this region is not part of the Daimler-Benz Rockwell-C method yet may give some additional insights. While for the conventional PAD film, surface flaking is visible due to the occurrence of very

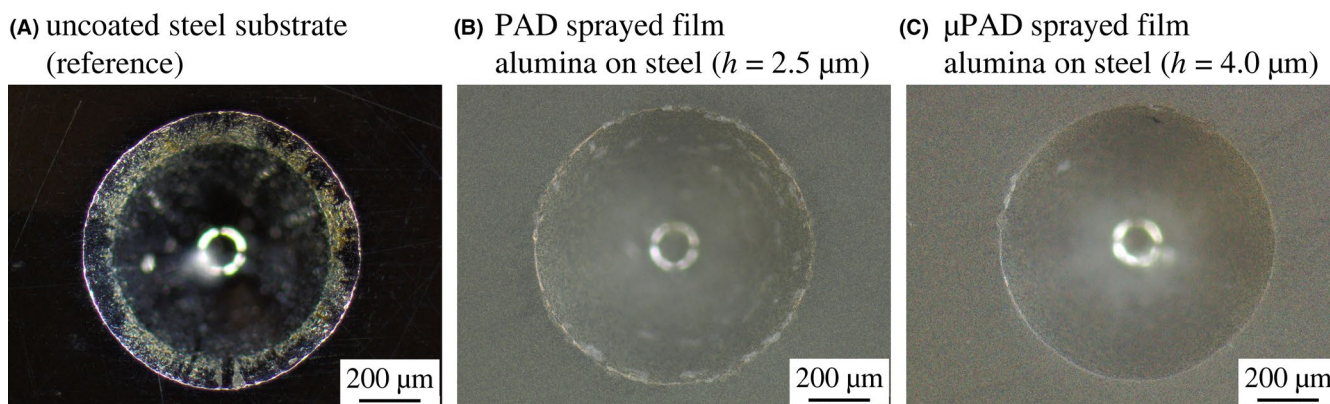


FIGURE 9 Optical microscope images of the indentation spot after evaluation in accordance with VDI 3198: (A) uncoated steel substrate, (B) PAD alumina film ($h = 2.5$ μm), and (C) μPAD alumina film ($h = 4.0$ μm) [Color figure can be viewed at wileyonlinelibrary.com]

high strain, little to no delamination is observed for the μ PAD films (despite their 1.5 μm higher film thickness). The cross-sectional SEM image of an indentation spot of a conventional PAD alumina film in Figure S8 (Supporting Information) supports the previous observations. At the edge as well as the complete surrounding of the imprint, the PAD film is still fully intact and free of delamination after testing. However, within the boundaries of the imprint, cracks in the film orientated perpendicular and parallel to the deformed surface become apparent. These cracks indicate that the applied high stresses exceed the stability of the PAD film and eventually lead to the optically observed surface flaking. For further testing of the crack formation in this region, indentation experiments were performed on an even thicker PAD film with $h = 8 \mu\text{m}$, hence substantially exceeding the specification of VDI 3198 ($h \leq 5 \mu\text{m}$). While delaminations begin to form at the surrounding of the imprint as expected due to the very high film thickness, the level of flaking within the center region nearly remains the same. The concentration of cracks in the SEM images is increased and pronounced perpendicular cracks appear, yet film adhesion and general integrity of the PAD film are still present. Returning to the optical examination of the imprints, μ PAD films may exhibit an even higher adhesion and mechanical strength than conventional PAD films; however, this initial observation needs further proof in future experiments.

Fracture resistance and excellent adhesion are based on multiple aspects of powder aerosol deposited films, namely.

1. a seamless interface between the substrate and the film that is free of cracks and delamination, known as *anchoring layer*: first impacting particles deform the substrate surface and may even get partially embedded, thereby increasing the substrate roughness and total interface area. Consequently, this roughened yet dense interface (typical in the height range of 200 nm to 700 nm) supports a mechanical clamping.^{64,65} Additionally, interactions in the form of ionic and covalent bonding between metallic atoms of the substrate and oxide ions from the alumina PAD film have been reported, that may also improve the film adhesion.⁶⁶
2. a high, near theoretical film density: the nanocrystalline, dense microstructure without pores, except for some nanopores, improves the cohesion of the coating material within the film.²
3. a static compressive pre-strain within powder aerosol deposited films. It lowers tensile stress levels when a tensile load is applied.

While the first two points are self-explaining, the last statement requires further explanation. The underlying deposition mechanism of PAD, typically referred to as

room temperature impact consolidation (RTIC), generates a nanocrystalline microstructure that is under a high compressive microstrain in the range of 0.5%–1.0%.^{29,67} Stresses can reach up to 2 GPa and are even be visible on a macroscopic scale since (thin) substrates get bended.⁶⁸ For alumina powders processed with oxygen as carrier gas; however, a lower macroscopic stress of 1 GPa is common.⁶⁸ This compressive stress seems undesirable at first glance, since it may cause a film peel-off at very high film thicknesses. However, technical ceramics sustain a considerably higher compressive strength compared to their tensile strength, commonly by one order of magnitude, so they are significantly more vulnerable to tensile strains. This basically means that compressive strains in PAD films are acceptable as long as the substrate–film interface (anchoring layer) is stable enough to withstand the formed stress. When a mechanical load is applied to PAD films, a superposition of the process-related compressive pre-strain and the additionally applied strain occurs. Hence, a tensile deformation applied to the PAD film first must relieve this pre-strain before a tensile stress state can build up. Since crack formation and propagation in brittle materials like glass and ceramics mainly occur under tensile stresses, the described pre-existing compression helps to suppress cracking that leads to the total failure of the coating. A similar behavior is well known for tempered/toughened glass panes, where tempering puts the outer glass surface into compression. This helps to increase mechanical strength by preventing the crack expansion and propagation that otherwise occurs at surface flaws.

For PAD as well as for μ PAD films, the highly dense and seamless substrate–film interface in combination with the explained process-related compressive strains cause the extraordinary hardness and tolerance to indentation or applied mechanical bending.

3.4 | Crystalline film properties

X-ray diffraction pattern of the powder and of the PAD/ μ PAD films deposited on silicon are shown in Figure 10. All reflections of the powder belong to the phase-pure α -alumina. Both, the PAD and the μ PAD film, have identical reflection positions and thus are also present as α -alumina.

Whereas the reflections of the powder show a distinctive, narrow shape, the reflections of the PAD/ μ PAD processed films are notably broadened. This behavior is well known for PAD films, since the RTIC mechanism is based on a fracturing of particles and crystallites upon impact combined with the already explained formation of microstrain.^{6,69} Rietveld refinement enables to calculate the crystallite sizes as well as the microstrain (see Table 3).

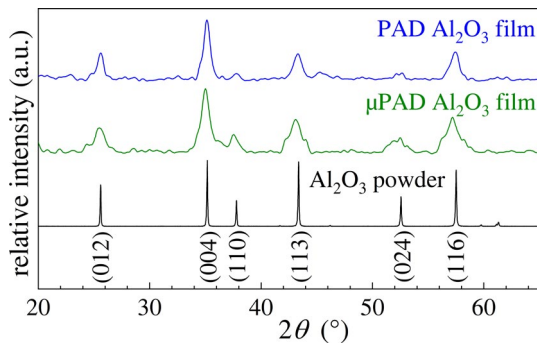


FIGURE 10 XRD pattern of the alumina powder and therefrom sprayed PAD and μ PAD films on silicon substrates [Color figure can be viewed at wileyonlinelibrary.com]

TABLE 3 Crystallite sizes and microstrain of sprayed alumina films on silicon substrates and the therefore used powder

	Powder	Conventional PAD	μ PAD
Crystallite size	180 nm	32 nm	16 nm
Microstrain	0.02%	0.62%	0.63%

The used α -alumina powders have a crystallite size of 180 nm with almost no microstrain (only 0.02%). The film manufactured by conventional PAD exhibits a decreased crystallite size of 32 nm and a high microstrain of 0.63%. When compared to the μ PAD film, both samples show a nearly identical microstrain; however, the crystallite size in case of μ PAD is even further reduced to 16 nm. So, the general behavior of both films indicates the presence of the RTIC mechanism with a reduced crystallite size and the formation of large strain. Yet, a significant difference occurs in respect to the crystallite dimensions after deposition. For PAD, the crystallite gets reduced by a factor of 5.6 (180 nm down to 32 nm), while for μ PAD this quotient is doubled to 11.2. This indicates that fracturing, and consequently consolidation, in case of μ PAD occurs more pronouncedly than for PAD. Since we believe this difference may actual be the key to explain changes in film properties between PAD and μ PAD, a detailed discussion of possible reasons is necessary. To our knowledge, neither the slight modification of the aerosol generation setup nor the miniaturized and modified deposition chamber are able to explain this large change in the film deposition behavior for μ PAD. Also, pressure levels can be ruled out as a major influencing factor, because identical aerosol generator pressures of 210 mbar were set for PAD as well as μ PAD, and the deposition chamber pressure is only slightly higher when comparing μ PAD to PAD (see Table 1). However, the main difference between both PAD variations is indeed the applied nozzle. Spot deposition as used in μ PAD required a nozzle with a larger deposition area, since the

film area cannot be increased through a substrate movement. When designing the nozzle, also higher and more flexible nozzle-to-substrate working distances were intended to improve the general usability and flexibility of the μ PAD device. As we considered, these requirements could only be met by de-Laval-type nozzles (converging-diverging nozzles). In addition, the converging-diverging layout enables to reach gas velocities above Mach 1 (velocity of sound). Consequently, also the powder within the particle-laden gas gets accelerated to higher particle velocities.^{70–72} In contrast, the barrel-type slit nozzle as used for conventional PAD only makes use of a converging layout and hence is physically limited to a velocity of about Mach 1. We strongly assume that in fact these higher particle velocities as created by de-Laval-nozzles lead to the improved deposition behavior for powder aerosol deposition. This agrees with observations of Naoe et al. and Kwon et al. made for the deposition of alumina particles.^{10,60} Although it is not possible to directly determine the particle velocity in-situ using our current devices, we plan to address this aspect in detail in our future work using the time-of-flight method as proposed by various groups.^{73,74}

The results not only show that the proposed μ PAD setup forms films with the typical crystalline reflection pattern of powder aerosol deposited films. Moreover, the de-Laval-type nozzle, which was used to enable the spot deposition in case of μ PAD, may even be responsible for the enhanced mechanical film properties compared to standard PAD films. This clearly underlines the high importance of the nozzle type and its geometry for PAD-based ceramic spray coating processes. Knowhow and advances in this field found for μ PAD may also benefit the conventional PAD to improve the deposition rate and efficiency here as well.

3.5 | Optical film properties

Since alumina films are often used as transparent protective films,^{75,76} optical properties like the transmittance T may be of high importance. Four films on glass substrates were prepared each by PAD and μ PAD with coating times t_c of 15, 30, 45, and 60 s, respectively. For transmittance evaluation, the measuring spot with a size of about 1 mm² was positioned to the center of the film, where a nearly constant film thickness is present (especially necessary in case of the bell-shaped μ PAD films). Due to varying deposition rates and film profiles of PAD and μ PAD, resulting film thicknesses also deviate for corresponding coating times. Hence, transmittance measurements of films with a thickness of 1.0, 1.6, 2.0, and 3.0 μ m for PAD were compared to μ PAD with thicknesses of 2.5, 5.0, 7.3, and 11 μ m (Figure 11A,B).

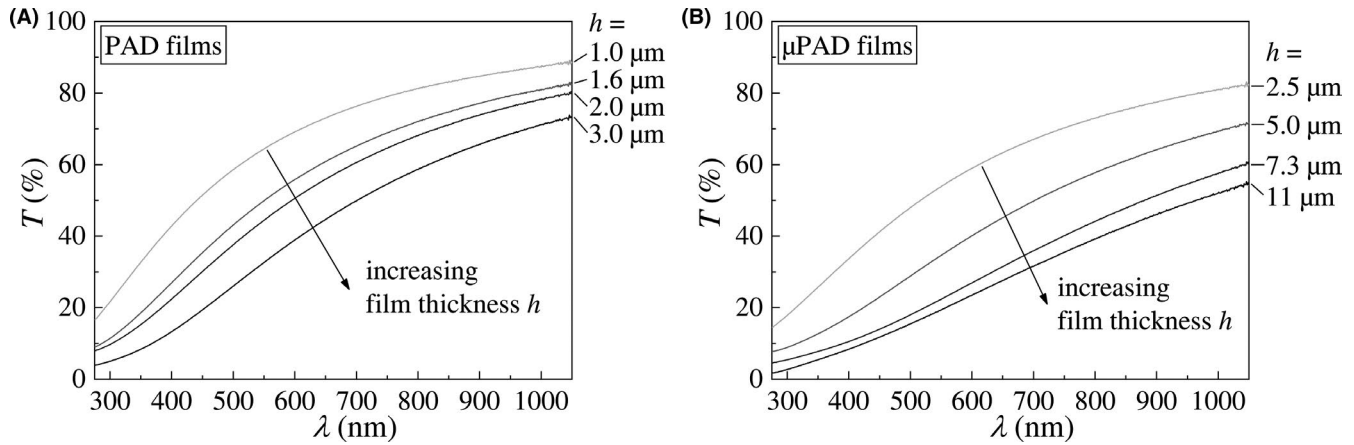


FIGURE 11 Optical transmittance T of films produced by (A) PAD and (B) μ PAD films depending on their film thickness h and wavelength λ

At first sight, two obvious results can be drawn: First, all films in general exhibit the same influence of λ on T . Whereas the highest transmittance T occurs at the highest measured wavelengths in the infrared region, T continuously decreases in the direction of smaller wavelengths λ . Within the UV region, films exhibit only a low transmittance, as also observed for bulk sapphire (single crystalline alumina). This λ -dependent behavior of the transmittance is typically for alumina in the form of both bulk samples and films.^{77,78} Second, by increasing the film thickness h , the transmittance T becomes lower. For larger film thicknesses, the light also travels for longer periods of time within the film, hence increasing the probability of interactions like scattering, absorbance, or reflection. Consequently, the transmittance decreases as observed when passing through thicker films in accordance with the Lambert–Beer law.

When looking more closely to the course of the transmittance, two regions with different slopes are visible especially for the thinner films. At smaller wavelengths, within the violet to green region of the light (400–550 nm), a steep incline occurs. In contrast, at higher wavelengths in the red to infrared region above 800 nm, only a smaller slope is visible. On the contrary, for higher film thicknesses, the course resembles more the form of a straight line without pronounced regions. A similar behavior was found by Kim et al. for bulk alumina disks when sintered at different temperatures.⁷⁹ However, the interactions of light in alumina like scattering are rather complex, since the grain size of the bulk alumina as well as pore size and concentration may affect the optical transmittance. Scattering of light mainly occurs at scattering centers like mentioned pores and grain boundaries. The latter is a consequence of birefringent that takes place in non-cubic ceramics like alumina due to differences in the direction-dependent refractive index.⁸⁰ PAD and μ PAD films feature

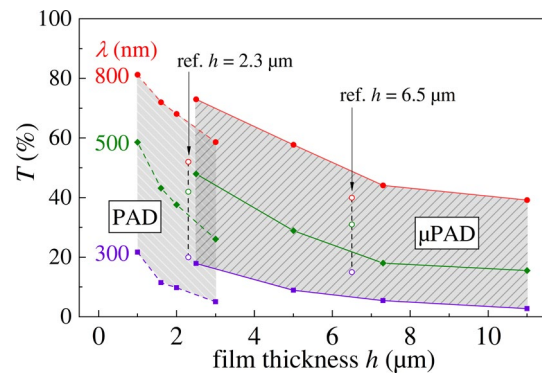


FIGURE 12 Comparison of the optical transmittance T of PAD and μ PAD films depending on their film thickness h and measured wavelength λ . Two alumina films produced by vacuum kinetic spraying with a thickness of 2.3 and 6.5 μm are given as reference (measured at identical wavelengths as PAD films)⁸⁰ [Color figure can be viewed at wileyonlinelibrary.com]

nanometer-sized grains combined with a very low concentration of nanopores as discussed in Section 3.2. This should be beneficial for high transmittance values.⁸¹

The transmittance T of all films manufactured by PAD and μ PAD is compared in respect to their film thickness in Figure 12. Wavelengths of 300, 500, and 800 nm are marked within the figure. Results from Lee et al. with 2.3 and 6.5- μm -thick alumina films produced by vacuum kinetic spraying (similar to PAD) at identical wavelengths are given as reference.

For both PAD and μ PAD, the already explained optical behavior already explained is evident: the optical transmittance T lowers with decreasing wavelength λ and increasing film thickness h . Of special interest is the thickness range between 2.5 and 3 μm , since results of PAD and μ PAD overlap and enable a direct comparison. Here, the film produced by μ PAD offers at least 10% higher transmittances than the conventional sprayed film and even

exceed a leap of 15% at $\lambda = 500$ nm. The transmittance of the corresponding PAD film was calculated by linear interpolation using the 2.0 and 3.0- μm -thick film. This increased transmittance of μPAD films may again be attributed to the increased film consolidation as discussed in Sections 3.2 and 3.4. Grains that are half the size of those in PAD films scatter light to a smaller extent,^{80,82} further assisted by a better consolidation with less and/or smaller pores. Alumina films reported in literature show a smaller wavelength-dependent variation of the transmittance, yet roughly coincide with films in this work.⁸³ For the 2.3- μm -thick film from ref. [77], T at $\lambda = 300$ nm closely matches the value of the 2.5- μm -thick μPAD film, whereas at $\lambda = 800$ nm it falls about 20% behind the μPAD film. For the thicker reference film with $h = 6.5$ μm , the relative levels are slightly shifted. Here, the reference film surpasses the μPAD film at $\lambda = 300$ nm by 9%, yet again falls back at $\lambda = 800$ nm by 9%. The difference in absolute transmittance between films in this work produced by PAD and μPAD , respectively, and data from literature may be explained by differing spray conditions and a different used alumina powder.

4 | CONCLUSION

Powder aerosol deposition is a promising technique to deposit dense ceramic films directly at room temperature. While previous developments pointed towards larger and more complex deposition devices, we followed a different approach and proposed a simplified and miniaturized device. The aim was twofold: creating a smaller, inexpensive, flexible, easily cleanable, and even mobile aerosol generation unit and deposition chamber with a low areal footprint (e.g., that fits in a glove box) as well as lowering the hurdle for other researchers to use powder aerosol deposition themselves. It should also be possible to deposit materials that are not available in large quantities. Therefore, we introduced a deposition chamber based only on commercially available small flange components and pipe/hose connections. Furthermore, we have deliberately avoided the use of electronically controlled equipment requiring additionally control hardware like a computer. Instead, manually operated devices like flow meters and manual valves were installed. A key point is the elimination of moving components by just using a spot deposition that was enabled by using a circular de-Laval-type nozzle. To distinguish this miniaturized setup, we introduced the term micropowder aerosol deposition, abbreviated as μPAD . The operational capability was proven for the deposition of alumina films and compared to conventional PAD in terms of mechanical, crystalline, and optical film properties.

Thick films with a bell-shaped-like profile were easily deposited by μPAD , featuring a plateau in the center of the films with a diameter of 5 mm and a FWHM diameter of about 10 mm. The obtained μPAD films do not only match the properties of the corresponding PAD films, but oftentimes outperformed them. Here, μPAD films exhibit increased hardness and optical transmittance values, surpassing reference values of the conventional sprayed counterparts by at least by 10%. Also, film integrity and adhesion to the substrate might be slightly higher in case of μPAD . Reasons for the improved film properties were found by X-ray diffraction with a significantly higher fracturing of impacting particles during μPAD combined with improved film consolidation. This was achieved by using a de-Laval-type nozzle for the spot deposition. Again, this underlines the importance of a suitable nozzle layout and may also enhance the deposition of conventional PAD. Consequently, μPAD featured doubled to tripled deposition rates and a nearly doubled deposition efficiency.

We believe that the proposed miniaturized μPAD device enables a flexible usage of the powder aerosol deposition method in the field of research and development as well as in new applications like the remanufacturing of partially damaged ceramic surface coatings.

COMPETING INTEREST

The authors declare no competing financial interest.

ACKNOWLEDGEMENTS

The authors are indebted to Mrs. Nicole Hall and the Bavarian Polymer Institute (KeyLab Electron and Optical Microscopy) for SEM imaging, the chair of metals and alloys (Prof. Uwe Glatzel, Hans Lassner-Meisel) for XRD, film adhesion, and microhardness measurements as well as to Dr. Martin Hämmerle for the optical transmittance measurements. Special thanks to Philipp Nieke for the development and provision of the de-Laval-type nozzles (greetings to NZ). Open Access funding enabled and organized by Projekt DEAL.

AUTHOR CONTRIBUTIONS

J.E. conceived, designed, and performed the experiments and subsequently analyzed the data and evaluated the results. M.L. and J.E. discussed the experimental design and all authors discussed the data jointly. J.K. and R.M. supervised the work. J.E. and R.M. wrote the manuscript. All authors have given approval to the final version of the manuscript.

ASSOCIATED CONTENT

Supporting Information: The following additional data and information are available in the SI: A detailed 3D model of the used μPAD apparatus; a schema of the PAD method; measurements regarding the deposition chamber

pressure; 3D film thickness measurements of films on glass substrates; a test chart and all measurements of the VDI 3198 indentation adhesion method; SEM images of selected indentation spots of PAD films; a complete sample list with coating parameters.

ORCID

Jörg Exner  <https://orcid.org/0000-0002-1601-2968>

Jaroslav Kita  <https://orcid.org/0000-0001-7063-9828>

Ralf Moos  <https://orcid.org/0000-0001-7622-0120>

REFERENCES

- Maria J-P, Kang X, Floyd RD, Dickey EC, Guo H, Guo J, et al. Cold sintering: current status and prospects. *J Mater Res.* 2017;32:3205–18. <https://doi.org/10.1557/jmr.2017.262>
- Hanft D, Exner J, Schubert M, Stöcker T, Fuierer P, Moos R. An overview of the aerosol deposition method: process fundamentals and new trends in materials applications. *J Ceram Sci Technol.* 2015;6:147–82. <https://doi.org/10.4416/jcst2015-00018>
- Guo J, Floyd R, Lowum S, Maria J-P, Herisson de Beauvoir T, Seo J-H, et al. Cold sintering: progress, challenges, and future opportunities. *Annu Rev Mater Res.* 2019;49:275–95. <https://doi.org/10.1146/annurev-matsci-070218-010041>
- Akedo J. Aerosol deposition (AD) integration techniques and their application to microdevices. In: Singh M, Ohji T, Asthana R, Mathur S, editors. *Ceramic integration and joining technologies.* Hoboken, NJ, USA: John Wiley & Sons, Inc; 2011. p. 489–520.
- Vardelle A, Moreau C, Akedo J, Ashrafizadeh H, Berndt CC, Berghaus JO, et al. The 2016 thermal spray roadmap. *J Therm Spray Technol.* 2016;25:1376–440. <https://doi.org/10.1007/s11666-016-0473-x>
- Exner J, Nazarenus T, Kita J, Moos R. Dense Y-doped ion conducting perovskite films of BaZrO₃, BaSnO₃ and BaCeO₃ for SOFC applications produced by powder aerosol deposition at room temperature. *Int J Hydrogen Energy.* 2020;45:10000–16. <https://doi.org/10.1016/j.ijhydene.2020.01.164>
- Kwon H, Kim Y, Park H, Lee C. The importance of intimate inter-crystallite bonding for the plasma erosion resistance of vacuum kinetic sprayed Y₂O₃ coating. *Surf Coat Technol.* 2019;374:493–9. <https://doi.org/10.1016/j.surfcoat.2019.05.052>
- Wang L-S, Zhou H-F, Zhang K-J, Wang Y-Y, Li C-X, Luo X-T, et al. Effect of the powder particle structure and substrate hardness during vacuum cold spraying of Al₂O₃. *Ceram Int.* 2016;43:4390–8. <https://doi.org/10.1016/j.ceramint.2016.12.085>
- Akedo J. Aerosol deposition of ceramic thick films at room temperature: densification mechanism of ceramic layers. *J Am Ceram Soc.* 2006;89:1834–9. <https://doi.org/10.1111/j.1551-2916.2006.01030.x>
- Kwon H, Kim Y, Park H, Lee C. Impact behavior for successful particle-particle bonding in vacuum kinetic spraying. *J Therm Spray Technol.* 2020. <https://doi.org/10.1007/s11666-020-01078-7>
- Kim JO, Choi WY, Choi BK, Jeong JT. Fabrication of photocatalytic TiO₂ thin film using innovative aerosol deposition method. *Mater Sci Forum.* 2006;510–511:1–4. <https://doi.org/10.4028/www.scientific.net/MSF.510-511.1>
- Yang G-J, Li C-J, Fan S-Q, Wang Y-Y, Li C-X. Influence of annealing on photocatalytic performance and adhesion of vacuum cold-sprayed nanostructured TiO₂ coating. *J Therm Spray Technol.* 2007;16:873–80. <https://doi.org/10.1007/s11666-007-9109-5>
- Ryu J, Park D-S, Hahn B-D, Choi J-J, Yoon W-H, Kim K-Y, et al. Photocatalytic TiO₂ thin films by aerosol-deposition: From micron-sized particles to nano-grained thin film at room temperature. *Appl Catal B.* 2008;83:1–7. <https://doi.org/10.1016/j.apcatb.2008.01.020>
- Park J-J, Kim D-Y, Lee J-G, Cha Y-H, Swihart MT, Yoon S. Supersonic aerosol-deposited TiO₂ photoelectrodes for photoelectrochemical solar water splitting. *RSC Adv.* 2014;4:8661–70. <https://doi.org/10.1039/C3RA47998F>
- Imanaka Y, Anazawa T, Manabe T, Amada H, Ido S, Kumasaka F, et al. An artificial photosynthesis anode electrode composed of a nanoparticulate photocatalyst film in a visible light responsive GaN-ZnO solid solution system. *Sci Rep.* 2016;6:35593. <https://doi.org/10.1038/srep35593>
- Exner J, Fuierer P, Moos R. Aerosol codeposition of ceramics: mixtures of Bi₂O₃-TiO₂ and Bi₂O₃-V₂O₅. *J Am Ceram Soc.* 2014;98:717–23. <https://doi.org/10.1111/jace.13364>
- Choi J-J, Ryu J, Hahn B-D, Ahn C-W, Kim J-W, Yoon W-H, et al. Low temperature preparation and characterization of solid oxide fuel cells on FeCr-based alloy support by aerosol deposition. *Int J Hydrogen Energy.* 2014;39:12878–83. <https://doi.org/10.1016/j.ijhydene.2014.06.070>
- Bredikhin SI, Agarkov DA, Agarkova E, Burmistrov I, Cherkasov A, Pukha V, et al. Aerosol deposition as a promising technique to fabricating a thin-film solid electrolyte of solid oxide fuel cells. *ECS Trans.* 2019;91:403–13. <https://doi.org/10.1149/09101.0403ecst>
- Wang L-S, Li C-X, Li G-R, Yang G-J, Zhang S-L, Li C-J. Enhanced sintering behavior of LSGM electrolyte and its performance for solid oxide fuel cells deposited by vacuum cold spray. *J Eur Ceram Soc.* 2017;37:4751–61. <https://doi.org/10.1016/j.jeurceramsoc.2017.06.007>
- Lim H-T, Yang C, Hwang SC, Choi Y-J. Experimental study of internal reforming on large-area anode supported solid oxide fuel cells. *Fuel Cells.* 2015;15:555–65. <https://doi.org/10.1002/fuce.201400070>
- Bae H, Choi J, Kim KJ, Park D, Choi GM. Low-temperature fabrication of protonic ceramic fuel cells with BaZr_{0.8}Y_{0.2}O_{3-δ} electrolytes coated by aerosol deposition method. *Int J Hydrogen Energy.* 2015;40:2775–84. <https://doi.org/10.1016/j.ijhydene.2014.12.046>
- Exner J, Pöpke H, Fuchs F-M, Kita J, Moos R. Annealing of gadolinium-doped ceria (GDC) films produced by the aerosol deposition method. *Materials.* 2018;11:2072. <https://doi.org/10.3390/ma11112072>
- Baba S, Sato H, Huang L, Uritani A, Funahashi R, Akedo J. Formation and characterization of polyethylene terephthalate-based (Bi_{0.15}Sb_{0.85})₂Te₃ thermoelectric modules with CoSb₃ adhesion layer by aerosol deposition. *J Alloys Compd.* 2014;589:56–60. <https://doi.org/10.1016/j.jallcom.2013.11.180>
- Nazarenus T, Kita J, Moos R, Exner J. Laser-annealing of thermoelectric CuFe_{0.98}Sn_{0.02}O₂ films produced by powder aerosol deposition method. *Adv Mater Interfaces.* 2020;7:2001114. <https://doi.org/10.1002/admi.202001114>
- Nazarenus T, Sun Y, Exner J, Kita J, Moos R. Powder aerosol deposition as a method to produce garnet-type solid ceramic

- electrolytes: a study on electrochemical film properties and industrial application. *Energy Technol.* 2021;2100211 (accepted). <https://doi.org/10.1002/ente.202100211>
26. Choi J-J, Ahn C-W, Ryu J, Hahn B-D, Kim J-W, Yoon W-H, et al. Li-ion conducting $\text{Li}_{0.35}\text{La}_{0.55}\text{TiO}_3$ electrolyte thick films fabricated by aerosol deposition. *J Korean Phys Soc.* 2016;68:12–6. <https://doi.org/10.3938/jkps.68.12>
 27. Kato T, Iwasaki S, Ishii Y, Motoyama M, West WC, Yamamoto Y, et al. Preparation of thick-film electrode-solid electrolyte composites on $\text{Li}_7\text{La}_3\text{Zr}_2\text{O}_{12}$ and their electrochemical properties. *J Power Sources.* 2016;303:65–72. <https://doi.org/10.1016/j.jpowsour.2015.10.101>
 28. Moritaka T, Yamashita Y, Tojo T, Inada R, Sakurai Y. Characterization of Sn_4P_3 -carbon composite films for lithium-ion battery anode fabricated by aerosol deposition. *Nanomaterials.* 2019;9:1032. <https://doi.org/10.3390/nano9071032>
 29. Hanft D, Exner J, Moos R. Thick-films of garnet-type lithium ion conductor prepared by the aerosol deposition method: the role of morphology and annealing treatment on the ionic conductivity. *J Power Sources.* 2017;361:61–9. <https://doi.org/10.1016/j.jpowsour.2017.06.061>
 30. Esaka T, Sakaguchi H, Miyashita Y. High rate performance of aerosol-deposited Mg_2Ge alloy anode in lithium batteries. *Electrochemistry.* 2010;78:611–4. <https://doi.org/10.5796/electrochemistry.78.611>
 31. Ahn C-W, Choi J-J, Ryu J, Hahn B-D, Kim J-W, Yoon W-H, et al. Microstructure and electrochemical properties of graphite and C-coated LiFePO_4 films fabricated by aerosol deposition method for Li ion battery. *Carbon.* 2015;82:135–42. <https://doi.org/10.1016/j.carbon.2014.10.043>
 32. Takai S, Sakaguchi H, Tanaka K, Nagao Y, Esaka T. Cathode performance of LiMn_2O_4 thick films prepared by gas-deposition for lithium rechargeable battery. *Electrochemistry.* 2008;76:293–6. <https://doi.org/10.5796/electrochemistry.76.293>
 33. Bektas M, Stöcker T, Mergner A, Hagen G, Moos R. Combined resistive and thermoelectric oxygen sensor with almost temperature-independent characteristics. *J Sens Sens Syst.* 2018;7:289–97. <https://doi.org/10.5194/jsss-7-289-2018>
 34. Kim E-S, Liang J-G, Wang C, Cho M-Y, Oh J-M, Kim N-Y. Interdigital capacitors with aerosol-deposited high-K dielectric layer for highest capacitance value in capacitive super-sensing applications. *Sci Rep.* 2019;9:680. <https://doi.org/10.1038/s41598-018-37416-7>
 35. Exner J, Schubert M, Hanft D, Stöcker T, Fuierer P, Moos R. Tuning of the electrical conductivity of $\text{Sr}(\text{Ti}, \text{Fe})\text{O}_3$ oxygen sensing films by aerosol co-deposition with Al_2O_3 . *Sens Actuators B.* 2016;230:427–33. <https://doi.org/10.1016/j.snb.2016.02.033>
 36. Liang J-G, Wang C, Yao Z, Liu M-Q, Kim H-K, Oh J-M, et al. Preparation of ultrasensitive humidity-sensing films by aerosol deposition. *ACS Appl Mater Interfaces.* 2018;10:851–63. <https://doi.org/10.1021/acsami.7b14082>
 37. Exner J, Albrecht G, Schönauer-Kamin D, Kita J, Moos R. Pulsed polarization-based NO_x sensors of YSZ films produced by the aerosol deposition method and by screen-printing. *Sensors.* 2017;17:1715. <https://doi.org/10.3390/s17081715>
 38. Sahnner K, Kaspar M, Moos R. Assessment of the novel aerosol deposition method for room temperature preparation of metal oxide gas sensor films. *Sens Actuators B.* 2009;139:394–9. <https://doi.org/10.1016/j.snb.2009.03.011>
 39. Akedo J. Room temperature impact consolidation (RTIC) of fine ceramic powder by aerosol deposition method and applications to microdevices. *J Therm Spray Technol.* 2008;17:181–98. <https://doi.org/10.1007/s11666-008-9163-7>
 40. Akedo J. Room temperature impact consolidation and application to ceramic coatings: aerosol deposition method. *J Ceram Soc Jpn.* 2020;128:101–16. <https://doi.org/10.2109/jcersj2.19196>
 41. Suzuki M, Tsuchiya T, Akedo J. Effect of starting powder morphology on film texture for bismuth layer-structured ferroelectrics prepared by aerosol deposition method. *Jpn J Appl Phys.* 2017;56(6S1):06GH02. <https://doi.org/10.7567/jjap.56.06gh02>
 42. Exner J, Schubert M, Hanft D, Kita J, Moos R. How to treat powders for the room temperature aerosol deposition method to avoid porous, low strength ceramic films. *J Eur Ceram Soc.* 2019;39:592–600. <https://doi.org/10.1016/j.jeurceramsoc.2018.08.008>
 43. Sarobol P, Chandross M, Carroll JD, Mook WM, Bufford DC, Boyce BL, et al. Room temperature deformation mechanisms of alumina particles observed from in situ micro-compression and atomistic simulations. *J Therm Spray Technol.* 2016;25:82–93. <https://doi.org/10.1007/s11666-015-0295-2>
 44. Kuroyanagi S, Shinoda K, Yumoto A, Akedo J. Size-dependent quasi brittle-ductile transition of single crystalline alpha-alumina particles during microcompression tests. *Acta Mater.* 2020;195:588–96. <https://doi.org/10.1016/j.actamat.2020.05.065>
 45. Akedo J, Ryu J, Jeong D-Y, Johnson SD. Aerosol deposition (AD) and Its applications for piezoelectric devices. *Advanced Piezoelectric Materials.* Elsevier. 2017;575–614.
 46. Imanaka Y. Materials and processes of microelectronic packaging including low-temperature cofired ceramics technology (past, present and future). *J Ceram Sci Technol.* 2015;6:291–300. <https://doi.org/10.4416/jcst2015-00050>
 47. Park J-J, Kim D-Y, Latthe SS, Lee J-G, Swihart MT, Yoon SS. Thermally induced superhydrophilicity in TiO_2 films prepared by supersonic aerosol deposition. *ACS Appl Mater Interfaces.* 2013;5:6155–60. <https://doi.org/10.1021/am401083y>
 48. Ryu J, Han G, Song TK, Welsh A, Trolrier-McKinstry S, Choi H, et al. Upshift of phase transition temperature in nanostructured PbTiO_3 thick film for high temperature applications. *ACS Appl Mater Interfaces.* 2014;6:11980–7. <https://doi.org/10.1021/am5000307>
 49. Patil DR, Annapureddy V, Kaarthik J, Thakre A, Akedo J, Ryu J. Piezoelectric thick film deposition via powder/granule spray in vacuum: a review. *Actuators.* 2020;9:59. <https://doi.org/10.3390/act9030059>
 50. Iwata A, Akedo J. Thickness Uniformity of Large Area PZT Films Formed by Aerosol Deposition. 16th IEEE International Symposium on Applications of Ferroelectrics 2007. Nara, Japan. doi: <https://doi.org/10.1109/ISAF.2007.4393294>
 51. Choi J-J, Park D-S, Seong B-G, Bae H. Low-temperature preparation of dense $(\text{Gd}, \text{Ce})\text{O}_{2-\delta}$ - Gd_2O_3 composite buffer layer by aerosol deposition for YSZ electrolyte-based SOFC. *Int J Hydrogen Energy.* 2012;37:9809–15. <https://doi.org/10.1016/j.ijhydene.2012.03.148>
 52. Hatono H, Ito T, Matsumura A. Technological Development of Aerosol Deposition at TOTO Ltd. 4th Tsukuba International Coatings Symposium - Frontiers of Coatings Technology: Innovative Processes and Applications 2010. Tsukuba, Japan.
 53. Palneedi H, Choi I, Kim G-Y, Annapureddy V, Maurya D, Priya S, et al. Tailoring the magnetoelectric properties of $\text{Pb}(\text{Zr}, \text{Ti})$

- O₃ film deposited on amorphous metglas foil by laser annealing. *J Am Ceram Soc.* 2016;99:2680–7. <https://doi.org/10.1111/jace.14270>
54. Exner J, Kita J, Moos R. In- and through-plane conductivity of 8YSZ films produced at room temperature by aerosol deposition. *J Mater Sci.* 2019;54:13619–34. <https://doi.org/10.1007/s10853-019-03844-7>
55. Exner J, Hahn M, Schubert M, Hanft D, Fuierer P, Moos R. Powder requirements for aerosol deposition of alumina films. *Adv Powder Technol.* 2015;26:1143–51. <https://doi.org/10.1016/j.apt.2015.05.016>
56. Williamson G, Hall W. X-ray line broadening from filed aluminium and wolfram. *Acta Metall.* 1953;1:22–31. [https://doi.org/10.1016/0001-6160\(53\)90006-6](https://doi.org/10.1016/0001-6160(53)90006-6)
57. Broitman E, Hultman L. Adhesion improvement of carbon-based coatings through a high ionization deposition technique. *J Phys: Conf Ser.* 2012;370:012009. <https://doi.org/10.1088/1742-6596/370/1/012009>
58. Kayali Y, Taktak S. Characterization and Rockwell-C adhesion properties of chromium-based borided steels. *J Adhes Sci Technol.* 2015;29:2065–75. <https://doi.org/10.1080/01694243.2015.1052617>
59. Vidakis N, Antoniadis A, Bilalis N. The VDI 3198 indentation test evaluation of a reliable qualitative control for layered compounds. *J Mater Process Technol.* 2003;143–144:481–5. [https://doi.org/10.1016/S0924-0136\(03\)00300-5](https://doi.org/10.1016/S0924-0136(03)00300-5)
60. Naoe K, Nishiki M, Yumoto A. Relationship between impact velocity of Al₂O₃ particles and deposition efficiency in aerosol deposition method. *J Therm Spray Technol.* 2013;22:1267–74. <https://doi.org/10.1007/s11666-013-0031-8>
61. Naoe K, Sato K, Nishiki M. Effect of process for producing Al₂O₃ particles on deposition efficiency in aerosol deposition method. *J Ceram Soc Jpn.* 2014;122:110–6. <https://doi.org/10.2109/jcersj2.122.110>
62. Lee D-W, Mi S. Factors affecting surface roughness of Al₂O₃ films deposited on Cu substrates by an aerosol deposition method. *J Ceram Process Res.* 2010;11:100–6.
63. Lee D-W, Kim H-J, Kim Y-H, Yun Y-H, Nam S-M. Growth process of α-Al₂O₃ ceramic films on metal substrates fabricated at room temperature by aerosol deposition. *J Am Ceram Soc.* 2011;94:3131–8. <https://doi.org/10.1111/j.1551-2916.2011.04493.x>
64. Kim J, Lee JI, Park DS, Park ES. Enhancement of interface anchoring and densification of Y₂O₃ coating by metal substrate manipulation in aerosol deposition process. *J Appl Phys.* 2015;117:14903. <https://doi.org/10.1063/1.4905241>
65. Schubert M, Hahn M, Exner J, Kita J, Moos R. Effect of substrate hardness and surface roughness on the film formation of aerosol-deposited ceramic films. *Funct Mater Lett.* 2017;10:1750045. <https://doi.org/10.1142/S179360471750045X>
66. Naoe K, Nishiki M, Sato K. Microstructure and electron energy-loss spectroscopy analysis of interface between Cu substrate and Al₂O₃ film formed by aerosol deposition method. *J Therm Spray Technol.* 2014;23:1333–8. <https://doi.org/10.1007/s11666-014-0172-4>
67. Exner J, Fuierer P, Moos R. Aerosol deposition of (Cu, Ti) substituted bismuth vanadate films. *Thin Solid Films.* 2014;573:185–90. <https://doi.org/10.1016/j.tsf.2014.11.037>
68. Schubert M, Exner J, Moos R. Influence of carrier gas composition on the stress of Al₂O₃ coatings prepared by the aerosol deposition method. *Materials.* 2014;7:5633–42. <https://doi.org/10.3390/ma7085633>
69. Exner J, Nazarenus T, Hanft D, Kita J, Moos R. What happens during thermal post-treatment of powder aerosol deposited functional ceramic films? Explanations based on an experiment-enhanced literature survey. *Adv Mater.* 2020;32:1908104. <https://doi.org/10.1002/adma.201908104>
70. Li C, Singh N, Andrews A, Olson BA, Schwartzentruber TE, Hogan CJ. Mass, momentum, and energy transfer in supersonic aerosol deposition processes. *Int J Heat Mass Transfer.* 2019;129:1161–71. <https://doi.org/10.1016/j.ijheatmasstransfer.2018.10.028>
71. Buhl S, Breuninger P, Antonyuk S. Optimization of a laval nozzle for energy-efficient cold spraying of microparticles. *Mater Manuf Processes.* 2017;33:1115–22. <https://doi.org/10.1080/10426914.2017.1279322>
72. Katanoda H, Fukuhara M, Iino N. Numerical simulation on impact velocity of ceramic particles propelled by supersonic nitrogen gas flow in vacuum chamber. *Mater Trans.* 2007;48:1463–8. <https://doi.org/10.2320/matertrans.T-MRA2007833>
73. Lebedev M, Akedo J, Mori K, Eiju T. Simple self-selective method of velocity measurement for particles in impact-based deposition. *J Vac Sci Technol A.* 2000;18:563–6. <https://doi.org/10.1116/1.582226>
74. Park H, Kwon J, Lee I, Lee C. Research on acceleration mechanism of in-flight particle and gas flow effect for the velocity control in vacuum kinetic spray process. *Korean J Mater Res.* 2014;24:98–104. <https://doi.org/10.3740/MRSK.2014.24.2.98>
75. Esther ACM, Sridhara N, Sebastian SV, Bera P, Anandan C, Aruna ST, et al. Optical and RF transparent protective alumina thin films. *J Mater Sci: Mater Electron.* 2015;26:9707–16. <https://doi.org/10.1007/s10854-015-3638-3>
76. Gottmann J, Kreutz EW. Pulsed laser deposition of alumina and zirconia thin films on polymers and glass as optical and protective coatings. *Surf Coat Technol.* 1999;116–119:1189–94. [https://doi.org/10.1016/S0257-8972\(99\)00191-7](https://doi.org/10.1016/S0257-8972(99)00191-7)
77. Yoshimura HN, de Camargo AC, Goulart EP, Maekawa K. Translucent polycrystalline alumina: influence of roughness and thickness on in-line transmittance. *Mater Sci Forum.* 1998;299–300:35–43. <https://doi.org/10.4028/www.scientific.net/MSF.299-300.35>
78. Lebedev M, Krumdieck S. Optically transparent, dense α-Al₂O₃ thick films deposited on glass at room temperature. *Curr Appl Physics.* 2008;8:233–6. <https://doi.org/10.1016/j.cap.2007.10.057>
79. Kim B-N, Hiraga K, Morita K, Yoshida H, Miyazaki T, Kagawa Y. Microstructure and optical properties of transparent alumina. *Acta Mater.* 2009;57:1319–26. <https://doi.org/10.1016/j.actamat.2008.11.010>
80. Wen T-C, Shetty DK. On the effect of birefringence on light transmission in polycrystalline magnesium fluoride. *J Am Ceram Soc.* 2015;98:829–37. <https://doi.org/10.1111/jace.13351>
81. Mata-Osoro G, Moya JS, Pecharroman C. Transparent alumina by vacuum sintering. *J Eur Ceram Soc.* 2012;32:2925–33. <https://doi.org/10.1016/j.jeurceramsoc.2012.02.039>
82. Yamashita I, Nagayama H, Tsukuma K. Transmission properties of translucent polycrystalline alumina. *J Am Ceram Soc.*

2008;91:2611–6. <https://doi.org/10.1111/j.1551-2916.2008.02527.x>

83. Lee C, Kim J, Park H, Nam J, Son KS, Im YT, et al. Effect of microstructural features on optical transmittance mechanism in vacuum kinetic sprayed Al_2O_3 film. Korean J Met Mater. 2016;54:15–21. <https://doi.org/10.3365/KJMM.2016.54.1.15>

SUPPORTING INFORMATION

Additional supporting information may be found online in the Supporting Information section.

How to cite this article: Exner J, Linz M, Kita J, Moos R. Making powder aerosol deposition accessible for small amounts: A novel and modular approach to produce dense ceramic films. Int J Appl Ceram Technol. 2021;18:2178–2196. <https://doi.org/10.1111/ijac.13841>